Research Square

Preprints are preliminary reports that have not undergone peer review.
They should not be considered conclusive, used to inform clinical practice,
or referenced by the media as validated information.

Genetic Gabrd Deficiency Drives Compensatory Myelination of Inhibitory Axons to Elevate Seizure Thresholds

Lishuo Liu
First Affiliated Hospital of Xi'an Jiaotong University
Xi Zhang
First Affiliated Hospital of Xi'an Jiaotong University
Qiang Meng
First Affiliated Hospital of Xi'an Jiaotong University
Haohao Cui
First Affiliated Hospital of Xi'an Jiaotong University
Xiaobo Ye
First Affiliated Hospital of Xi'an Jiaotong University
Yong Liu
First Affiliated Hospital of Xi'an Jiaotong University
Huanfa Li
First Affiliated Hospital of Xi'an Jiaotong University
Yutao Ren
First Affiliated Hospital of Xi'an Jiaotong University
Wei Wu
First Affiliated Hospital of Xi'an Jiaotong University
Hua Zhang
First Affiliated Hospital of Xi'an Jiaotong University
Hao Wu
wu_hao@xjtu.edu.cn

First Affiliated Hospital of Xi'an Jiaotong University

Research Article

Keywords: epilepsy, GABAA receptor δ subunit, parvalbumin, myelination, homeostatic compensation

Posted Date: June 25th, 2026

DOI: https://doi.org/10.21203/rs.3.rs-10024120/v1

License: This work is licensed under a Creative Commons Attribution 4.0 International License.
Read Full License

Additional Declarations: No competing interests reported.

Abstract

Background

Tonic inhibition mediated by extrasynaptic $GABA_A$ receptors containing the δ subunit (GABRD) is a critical regulator of neuronal excitability. While mutations or loss of *GABRD* are conventionally linked to network disinhibition and increased epilepsy susceptibility, we investigated a paradoxical observation that global *Gabrd* knockout (Gabrd-KO) mice display resistance to chemoconvulsant-induced seizures.

Methods

Multi-modal profiling was employed, including electroencephalography (EEG), c-Fos mapping, tandem mass tag (TMT)-based quantitative proteomics, and single-nucleus RNA sequencing (snRNA-seq), to evaluate seizure susceptibility and hippocampal microcircuit remodeling in Gabrd-KO mice. Developmental and adult-acquired epilepsy models were compared. Clemastine was administered during the critical maturation period of parvalbumin-positive (PV^+) interneurons to pharmacologically enhance myelination.

Results

Gabrd-KO mice exhibited profound resistance to chemoconvulsant-induced seizures, driven by homeostatic remodeling of hippocampal inhibitory circuits. This involved a compensatory expansion of the PV^+ interneuron pool and a selective, directional enhancement of PV^+ axonal myelination. Pleiotrophin (PTN) signaling was identified as the key mediator of this adaptive neuron–oligodendrocyte communication. Crucially, this compensation was strictly dependent on a developmental window and was absent in an adult-acquired epilepsy model. Pharmacological reinforcement of myelination with clemastine during PV^+ interneuron maturation phenocopied the seizure-resistant state observed in Gabrd-KO mice.

Conclusions

These findings uncover an endogenous program for excitation/inhibition homeostasis, whereby the brain counteracts inhibitory deficits through structural fortification of PV^+ interneuronal axons. This study provides a transformative therapeutic rationale for targeting myelination in refractory epilepsy.

Introduction

Physiological homeostasis of the central nervous system rests upon a precise dynamic balance between excitatory glutamatergic input and inhibitory γ-aminobutyric acid (GABA) transmission[1]. Within the

inhibitory microcircuits, parvalbumin-positive (PV^+) fast-spiking interneurons generate powerful postsynaptic inhibition. This allows for the millisecond-precise synchronization of principal neuron firing, establishing these interneurons as critical regulators of the excitatory/inhibitory (E/I) balance[2, 3]. Distinct from synaptically localized receptors that mediate phasic inhibition, δ-subunit (GABRD)-containing $GABA_A$ receptors are predominantly extrasynaptic and mediate persistent tonic inhibition[4]. Owing to their high affinity for ambient extracellular GABA and slow desensitization kinetics, δ-containing receptors provide a baseline inhibitory tone that regulates neuronal firing thresholds and controls overall network gain[5].

Given the central role of GABRD in inhibitory regulation[6], functional impairments in δ-subunit-containing $GABA_A$ receptors are conventionally considered to be associated with epilepsy[7]. Clinical genetic studies link *GABRD* mutations to juvenile myoclonic epilepsy (JME) and generalized epilepsy with febrile seizures plus (GEFS+)[8–10]. Downregulation of δ subunits in dentate granule cells has also been observed in experimental temporal lobe epilepsy models[11]. Consequently, the prevailing model posits that *Gabrd* loss impairs tonic inhibition, directly shifting the networks toward hyperexcitability and lowering the seizure threshold[12, 13]. However, while global *Gabrd* knockout (Gabrd-KO) mice display anxiety-like behaviors and cognitive deficits[14, 15], it remains poorly understood how the absence of δ-subunit-mediated inhibition influences system-level circuit architecture, or whether such a sustained deficit triggers endogenous homeostatic compensatory mechanisms.

In the present study, we investigate the systemic consequences of genetic *Gabrd* deficiency on network excitability. Using electroencephalography (EEG), c-Fos activity mapping, and behavioral assays, we demonstrate that Gabrd-KO mice unexpectedly exhibit a paradoxical seizure-resistant phenotype in chemically induced epilepsy models, an observation that diverges from the classical assumption that inhibitory receptor loss necessarily precipitates hyperexcitability. Integrative analyses of tandem mass tag (TMT) quantitative proteomics and single-nucleus RNA sequencing (snRNA-seq) further reveal that this resistance is driven by an endogenous compensatory mechanism. Specifically, *Gabrd* loss triggers inhibitory microcircuit remodeling characterized by an enhancement of axonal myelination in PV^+ interneurons. This structural adaptation increases the functional resilience of inhibitory circuits, thereby counteracting aberrant network synchrony. These findings elucidate a previously uncharacterized dimension of homeostatic plasticity and highlight PV^+ interneuron myelination as a potential structural target for therapeutic intervention in refractory epilepsy.

Methods

Animals and Ethics

Adult C57BL/6J mice (male and female, 20–25 g) were purchased from the Experimental Animal Center, School of Medicine, Xi'an Jiaotong University. *Gabrd* knockout (Gabrd-KO) mice (Cat# NM-KO-200604) were purchased from Shanghai Southern Model Biotechnology Co., Ltd. Animals were housed under

controlled conditions (22 ± 1°C, 12-h light/dark cycle, lights on at 07:00) with ad libitum access to food and water. This study strictly adhered to the Declaration of Helsinki and the relevant guidelines outlined in the Guide for the Care and Use of Laboratory Animals. All procedures were approved by the Ethics Review Committee of the First Affiliated Hospital of Xi'an Jiaotong University (approval No. LLSBPJ-2023-265). Throughout the animal experiments, animal welfare was prioritized as the primary principle. All procedures were performed by professionally trained personnel, and every effort was made to minimize pain and distress to the animals. The study design and implementation followed the guidelines of Animal Research: Reporting of In Vivo Experiments (ARRIVE) and the fundamental principles of the Basel Declaration (http://www.basel-declaration.org), while fully implementing the 3R principles of replacement, refinement, and reduction in animal use.

Chemoconvulsant-Induced Seizure Models and Seizure Assessment

Two distinct seizure models were utilized. For the pilocarpine model, mice were pretreated with scopolamine (1 mg/kg, i.p.) to limit peripheral cholinergic effects, followed 30 min later by pilocarpine (300 mg/kg, i.p.). Control mice were administered an equal volume of sterile saline. For the focal kainic acid (KA) model, 50 nL of 20 mM KA (in 0.9% NaCl) was stereotaxically microinjected into the right dorsal hippocampus (coordinates: 1.9 mm posterior to bregma, 1.5 mm lateral to the midline, and 1.9 mm ventral to the skull surface). Sham-operated control mice received an equal volume of sterile saline at the same coordinates. Seizure severity was monitored for 1 h post-injection and scored using a modified Racine scale: stages 1–2, characterized by facial automatisms, tail stiffness, and wet-dog shakes; stage 3, unilateral forelimb myoclonus; stage 4, bilateral forelimb myoclonus with rearing; and stage 5, generalized myoclonic-tonic seizures accompanied by loss of postural control.

Pharmacological Intervention

Clemastine (MCE, HY-B0298) was dissolved in distilled water (1 mg/mL). Wild-type and *Gabrd*$^{-/-}$ mice received daily intraperitoneal injections of vehicle or clemastine (10 mg/kg) starting from postnatal day 28 (P28). Seizure induction, behavioral assays, and tissue collection were performed 15 days after the initiation of treatment. Subsequently, brain tissues were collected for protein preparation and Western blotting, or fixed for cryosectioning and immunofluorescence staining.

Total Protein Preparation and Western Blotting

Mice were euthanized under deep isoflurane anesthesia (VETEASY, RWD Life Sciences). Brain regions (hippocampus, cortex, thalamus, and cerebellum) were rapidly dissected in ice-cold phosphate-buffered saline (PBS), and homogenized in radioimmunoprecipitation assay (RIPA) buffer (25 mM Tris-HCl, pH 7.6, 150 mM NaCl, 0.1% SDS, 1% NP-40, 1% sodium deoxycholate) supplemented with protease inhibitors (ThermoFisher, Cat#89901). The homogenates were centrifuged at 12,000 rpm for 20 min at 4°C. Protein

concentrations of the tissue lysates were quantified via the bicinchoninic acid (BCA) assay. The lysates were resolved by SDS-PAGE for subsequent Western blot analysis.

Immunofluorescence and Histology

Mice were anesthetized with isoflurane (VETEASY, RWD Life Sciences). Following transcardial perfusion with 4% paraformaldehyde (PFA), brains were post-fixed overnight and cryoprotected in a 15–30% sucrose gradient. Each brain was sectioned into 14-μm-thick coronal slices via cryostat. Tissue sections were permeabilized with 0.1% Triton X-100, blocked with 10% normal goat serum, and incubated overnight at 4°C with primary antibodies against GABRD (Abcam, Cat# 1043882-2), PV (Proteintech, Cat# 488-29812), NeuN (Merck Millipore, Cat# ABN90), c-Fos (Cell Signaling Technology, Cat# 2250S), and MBP (Proteintech, Cat# 10458-1-AP). Fluorescently labeled secondary antibodies were applied for 3 h at room temperature. For quantitative analysis of myelinated inhibitory axons, MBP^+ PV^+ axons were imaged in the hippocampus using a 60× oil-immersion objective and quantified as a percentage of total MBP^+ axons [16].

EEG Implantation, Recording, and Spectral Analysis

Mice were secured in a stereotaxic frame under isoflurane anesthesia (an induction concentration of 4% and a maintenance level of 1.5–2.5%). Cortical surface electrodes were implanted bilaterally over multiple brain regions for simultaneous EEG recording. Following a one-week recovery, EEG signals were acquired using Neuro Workbench software version 06.20.0000 (KODENSHI). During recording sessions, both resting-state EEG activity and EEG activity following drug induction were recorded. Raw EEG data were preprocessed in MATLAB R2024b (MathWorks, Cambridge, United Kingdom). First, band-pass filtering was applied to isolate the target EEG frequency bands: Delta (0.5–4 Hz), Theta (4–8 Hz), Alpha (8–13 Hz), Beta (13–30 Hz), Gamma (30–80 Hz), and the full frequency band (0.5–80 Hz). Subsequently, a notch filter with a 2-Hz stopband centered at 50 Hz and its harmonics was applied to each frequency band to remove environmental power-line interference. A specified reference electrode approach was employed to eliminate common-mode noise in the EEG signals. Finally, residual noise sources, including myogenic artifacts, ocular artifacts, and head movement artifacts, were removed using a combination of independent component analysis (ICA) and manual artifact rejection.

Power spectral density (PSD) of the EEG data was estimated using the multitaper method implemented in the Brainstorm toolbox[17]. To further characterize the spectral features of the EEG signals across the different frequency bands, the Fast Fourier Transform (FFT) was applied using a 4-second time window with 50% overlap to compute PSD. Absolute power for each frequency band was obtained by integrating the PSD over the respective frequency ranges. Changes in EEG power across the different frequency bands were compared before and after drug-induced seizure onset in mice.

Tandem Mass Tag Quantitative Proteomics

Snap-frozen brain tissues from wild-type and Gabrd-KO mice were ground under cryogenic conditions and lysed in buffer (8 M urea, 1% protease inhibitor cocktail) by ultrasonication on ice, and after centrifugation the supernatant was collected for BCA protein quantification. For each sample, 100 μg protein was precipitated with 25% trichloroacetic acid (TCA), washed with pre-chilled acetone, and reconstituted in 200 mM triethylammonium bicarbonate (TEAB). Proteins were reduced with 5 mM dithiothreitol (DTT) at 37°C for 1 h and alkylated with 11 mM iodoacetamide (IAM) in the dark at room temperature for 30 min. Trypsin was added at a 1:50 enzyme-to-substrate ratio (w/w) for overnight digestion at 37°C. The resulting peptides were desalted (C18 cartridge), resuspended in 0.5 M TEAB, and labeled with TMT reagents at room temperature for 2 h. Labeled samples were pooled, desalted, and fractionated by high-pH reverse-phase HPLC on an Agilent 300 Extend C18 column using an 8%–32% acetonitrile gradient over 60 min, yielding six fractions. LC-MS/MS analysis was performed on an EASY-nLC 1200 coupled to an Orbitrap Exploris 480 with data-dependent acquisition and HCD fragmentation (32% normalized collision energy; resolution: 120,000 for MS1, 45,000 for MS2). Raw data were processed with Proteome Discoverer (v2.4.1.15) against the mouse UniProt database (17,063 entries); fixed modifications: carbamidomethyl (C) and TMT6plex (N-term/K); variable: acetyl (N-term) and oxidation (M). Peptide and protein identifications were filtered at FDR ≤ 1%; differentially expressed proteins were defined by fold-change > 1.2 (or < 1/1.2) and $P < 0.05$ (two-tailed t-test); subsequent bioinformatics included GO, KEGG, subcellular localization, COG/KOG, and PPI network analysis. TMT labeling, LC-MS/MS acquisition, and bioinformatics were performed by PTM Biolabs, Inc. (Hangzhou, China).

Single-Cell RNA Sequencing and Library Construction

Single-cell RNA-seq libraries were prepared using the Smart-seq2 protocol. Hippocampal tissues from wild-type and Gabrd-KO mice (two animals per genotype) were dissociated into single-cell suspensions, and individual cells were manually picked into lysis buffer. Reverse transcription was performed using oligo (dT) primers and LNA-containing template-switching oligonucleotides (Exiqon). ERCC spike-in RNA controls (Ambion) were added at a 1:1,000,000 dilution to a randomly selected subset of samples from both genotypes. Full-length cDNA was amplified by 20 cycles of PCR using KAPA HiFi DNA polymerase (KAPA Biosystems), and each amplified cDNA was quantified and assessed on a high-sensitivity Bioanalyzer chip (Agilent); samples with undetectable or degraded cDNA (~ 10% of total) were excluded. Qualified cDNA was converted into Illumina sequencing libraries using the Nextera XT protocol (Illumina) with minor modifications, and sequenced on an Illumina HiSeq 2000 platform in paired-end mode. Raw reads were trimmed with Btrim and aligned to the mouse genome (ENSEMBL Release 78) using STAR (v2.4.0g). Gene-level counts were obtained with feature Counts, and normalized using the TMM method (edgeR). Principal component analysis (FactoMineR), hierarchical clustering (Euclidean distance or correlation coefficients), and differential expression analysis (likelihood ratio test, adjusted $P < 0.01$, Benjamini-Hochberg) were performed, followed by cell-cell communication inference with CellChat (v1.1.0). Library preparation, sequencing, and basic data processing were carried out by Jingneng Biotech Co., Ltd. (Shanghai, China).

Transmission Electron Microscopy

The corpus callosum and hippocampus were rapidly dissected and fixed in 2.5% glutaraldehyde (EM grade) overnight. Sample preparation and image acquisition were performed by Servicebio (Wuhan, China). The extent of axonal myelination was quantified by calculating the g-ratio, defined as the ratio of axon diameter to total fiber diameter (axon diameter plus myelin sheath thickness). Axon diameter measurements and axon counts were performed using ImageJ software.

Statistical Analysis

Differences in protein expression across multiple time points were analyzed using one-way analysis of variance (one-way ANOVA). Independent samples t-tests were employed to compare protein expression levels and fluorescence intensity between two groups. The Mann-Whitney U test was used to assess differences in seizure severity scores in drug-induced animals. Behavioral data on seizure latency following drug induction and EEG data between the two groups were analyzed using independent samples t-tests. Myelination-related parameters obtained from transmission electron microscopy were also compared between the two groups using independent samples t-tests. All data are presented as mean ± standard error of the mean (SEM). Statistical significance was set at $P < 0.05$. Detailed information regarding the specific statistical tests applied for each analysis is provided in the corresponding figure legends. All statistical analyses were performed using GraphPad Prism (version 8.3.0.538).

Results

Validation of the Gabrd-Deficient Mouse Model

To investigate the systemic consequences of δ-subunit loss, we characterized a global *Gabrd* knockout mouse line. Genomic deletion was confirmed via tail-clip genotyping (Fig. S1A – S1C). Given the critical roles of the hippocampus, cortex, cerebellum, and thalamus in seizure initiation and propagation, we first assessed GABRD protein expression across these regions using Western blot analysis. Quantitative immunoblotting demonstrated a complete absence of the δ-subunit in all analyzed brain regions of mice compared with wild-type (WT) mice (Fig. 1A, B). To evaluate the spatial distribution of the protein and its cellular localization, we performed double immunofluorescence labeling for GABRD and the neuronal marker NeuN. In WT mice, GABRD immunoreactivity was robustly detected in a region-specific manner within the hippocampus and cortex; this signal was entirely absent in Gabrd-KO mice (Fig. 1C – G). To ensure that the genetic deletion did not induce gross neuroanatomical abnormalities or developmental neuronal loss, we quantified $NeuN^+$ cell density across the target regions. No significant differences in neuronal density were observed between Gabrd-KO and WT mice (Fig. 1C – G), suggesting that the constitutive loss of δ-subunits does not alter baseline neuronal survival or primary anatomical structures. Collectively, these results validate the Gabrd-KO model as a robust tool for investigating the effects of chronic δ-subunit deficiency in the absence of confounding developmental neurodegeneration.

Gabrd Deficiency Elevates Seizure Thresholds and Attenuates Ictal Electrocortical Activity

To assess the impact of *Gabrd* deficiency on seizure susceptibility, we first monitored electrocorticographic (ECoG) activity following chemoconvulsant administration (Fig. 2A, B). Following intraperitoneal injection of pilocarpine, Gabrd-KO mice exhibited a significantly prolonged latency to the first epileptiform discharge and a marked reduction in discharge frequency within the 1-hour post-induction observation window compared with WT mice (Fig. 2D, E). Power spectral analysis revealed no statistically significant differences in absolute power across all frequency bands between the two groups under resting conditions, indicating that baseline cortical network activity was not fundamentally altered by *Gabrd* deletion (Fig. 2F). However, during ictal periods, Gabrd-KO mice displayed significantly lower power spectral density in the theta band (4–8 Hz), relative to WT mice (Fig. 2G). To corroborate these electrophysiological phenotypes behaviorally, we assessed seizure thresholds in two independent acute seizure models. In the systemic pilocarpine-induced model, Gabrd-KO mice displayed a significantly prolonged latency to reach generalized motor seizures (Racine stage 4) compared with WT mice (Fig. 2H). Similarly, in the focal seizure model utilizing stereotaxic intrahippocampal kainic acid (KA) microinjection, the latency to stage 4 seizures was also markedly extended in Gabrd-KO mice (Fig. 2I). Collectively, the electrophysiological and behavioral data establish that systemic *Gabrd* deficiency significantly increases tolerance to proconvulsant stimuli in mice.

Gabrd Deficiency Attenuates Seizure-Induced Neuronal Activation

To evaluate the extent of neuronal activation during seizures at the cellular level, we quantified the expression of the immediate early gene c-Fos. A preliminary time-course analysis in wild-type (WT) mice revealed that c-Fos immunoreactivity in both the hippocampus and cortex peaked at 4 hours post seizure onset (Fig. 3A, B). Based on this temporal profile, we selected the 4 h post-ictal time point to compare neuronal activation between WT and Gabrd-KO, utilizing cohorts matched for behavioral seizure severity. Quantitative immunofluorescence analysis showed that the density of c-Fos-positive neurons in both the hippocampus and cortex was significantly attenuated in Gabrd-KO mice relative to WT mice (Fig. 3D, E). These histological findings data align with the *in vivo* electrophysiological and behavioral phenotypes, indicating that *Gabrd* deletion blunts seizure-induced neuronal activation within the cortical-hippocampal network.

Quantitative Proteomics Identifies Upregulation of Parvalbumin and Myelin- Associated Proteins in the Gabrd-KO Hippocampus

To elucidate the molecular alterations associated with *Gabrd* deficiency, we performed TMT-based quantitative proteomic analysis on hippocampal tissues. Comparing Gabrd-KO and WT mice, we identified 108 differentially expressed proteins (DEPs) utilizing a threshold of fold change (FC) ≥ 1.2 and a false discovery rate (FDR) < 0.05, comprising 74 upregulated and 34 downregulated proteins (Fig. 4A, B). Gene Ontology (GO) enrichment analysis indicated that DEPs were highly enriched in pathways

associated with GABAergic synaptic transmission, protein metabolism, and myelin structure (Fig. 4C – E). To map the functional landscape of these alterations, we constructed a protein-protein interaction (PPI) network. The interactome revealed prominent clustering of upregulated nodes related to myelin composition and the complement C1q complex, alongside an expected attenuation in the GABA receptor complex node (Fig. 4F, G). Within these enriched modules, the expression of parvalbumin (PV), a primary marker of fast-spiking inhibitory neurons, and myelin basic protein (MBP), a major structural protein of myelin sheaths, was significantly elevated. Together, these proteomic signatures suggest that *Gabrd* deficiency may drive the molecular remodeling of local inhibitory microcircuits and myelin structure in the hippocampus, which may collectively contribute to the observed elevation in seizure thresholds.

Gabrd Deficiency Increases PV^+ Interneuron Density and Drives Targeted Axonal Hypermyelination

To validate the proteomic findings and assess their structural implications at the cellular level, we systematically analyzed protein abundance, cell density, and ultrastructural morphology. Quantitative immunoblotting confirmed that the expression levels of PV and MBP were significantly upregulated in the hippocampus of Gabrd-KO mice relative to WT mice (Fig. 5A–D). Consistent with the immunoblot data, quantitative immunofluorescence analysis revealed a significant increase in the density of PV^+ inhibitory interneurons within both the hippocampus and cortex of Gabrd-KO mice (Fig. 5E – G; Fig. S3A).

To determine whether the elevation in MBP corresponded to physical changes in myelination, we evaluated hippocampal ultrastructure using transmission electron microscopy (TEM). In the Gabrd-KO hippocampus, we observed an increased density of myelinated axons per unit area, accompanied by a significant enhancement in myelin sheath thickness, as quantified by g-ratio analysis (Fig. 5H, I). Notably, these ultrastructural alterations were region-specific, as comparable hypermyelination was absent in the adjacent white matter (corpus callosum; Fig. S4A, S4B). Furthermore, the density of mitochondria residing within these myelinated hippocampal axons was significantly increased in Gabrd-KO mice (Fig. 5J), suggesting an increased energetic demand associated with local structural remodeling. More critically, immunofluorescence co-localization analysis demonstrated a significant increase in the proportion of MBP-ensheathed PV^+ axons in both the CA1 and dentate gyrus (DG) regions of Gabrd-KO mice (Fig. 5K–M). Together, these results indicate that *Gabrd* deficiency induces fine structural remodeling of local hippocampal microcircuits, characterized by an increased density of inhibitory neurons and targeted hypermyelination of their axons.

Single-Nucleus Transcriptomics Reveals Global Intercellular Signaling Attenuation and PTN-Driven Myelinogenic Remodeling

To dissect the cellular mechanisms underlying hippocampal network remodeling in the absence of the δ-subunit, we performed single-nucleus RNA sequencing (snRNA-seq) on hippocampal tissues and conducted cell–cell communication analysis using the CellChat algorithm. The results showed that

global cell–cell communication was substantially attenuated in Gabrd-KO mice, with the total number and the overall strength of inferred signaling interactions reduced by more than 50% compared with WT mice (Fig. 6C).

Despite this widespread suppression of classical intercellular signaling, pathways associated with myelination, including platelet-derived growth factor (PDGF), myelin-associated glycoprotein (MAG), and endocannabinoid pathway, were relatively preserved (Fig. 6D). Further analysis revealed that signaling through the pleiotrophin (PTN) pathway, a recognized pro-myelinating factor, underwent significant subpopulation-specific upregulation in the Gabrd-KO hippocampus. Specifically, oligodendrocyte precursor cells (OPCs), astrocytes, and specific excitatory neuron subpopulations (C4, C8, C12), demonstrated enhanced PTN signaling output. Conversely, the agrin (AGRN) and junctional adhesion molecule (JAM) signaling pathways, which mediate synaptic stabilization and cell adhesion, were significantly impaired within specific excitatory neuron subpopulations (Fig. 6E, F). Together, these results suggest that *Gabrd* deficiency fundamentally shifts the hippocampal intercellular signaling landscape, broadly suppressing synapse- and adhesion-related pathways while selectively upregulating PTN-mediated myelinogenic signaling.

Acquired GABRD Downregulation in TLE Fails to Recapitulate the Cellular Remodeling Observed in Constitutive Knockout Mice

To investigate whether the microcircuit remodeling observed in constitutive *Gabrd* deficiency mice is also present in an acquired epilepsy model, we evaluated endogenous GABRD protein levels in a mouse model of temporal lobe epilepsy (TLE). Quantitative immunoblot analysis revealed that GABRD protein levels in both the hippocampus and cortex progressively and significantly decreased over the course of epileptogenesis (days 1, 7, and 28 post-status epilepticus) (Fig. 7A–D). However, in contrast to the constitutive knockout model, PV protein levels did not exhibit a corresponding upregulation during the pathological progression of TLE (Fig. 7E–H). Quantitative histological analysis further confirmed that despite the marked reduction of GABRD expression in the chronic phase of TLE (day 28), the density of PV^+ interneurons remained unchanged (Fig. 7I–M). These results indicate that the disease-associated, secondary downregulation of GABRD is insufficient to trigger the PV^+ interneuron expansion observed following congenital *Gabrd* deletion (Fig. 7I–M).

Pharmacological Induction of Myelination Elevates Seizure Thresholds and Phenocopies the Gabrd-KO Phenotype

To determine whether enhanced myelination is sufficient to confer seizure protection, WT mice were treated with the M1 muscarinic receptor antagonist clemastine, a known pro-myelinating agent, for 14 consecutive days initiated at either postnatal day 28 (P28). We first assessed functional outcomes using a chemoconvulsant-induced seizure model. *In vivo* behavioral assays demonstrated that clemastine-pretreated mice exhibited significantly prolonged seizure latency and elevated seizure thresholds compared with vehicle-treated controls (Fig. 8A). To corroborate these behavioral findings with

molecular changes, we examined hippocampal lysates. Clemastine administration significantly upregulated myelin basic protein (MBP) abundance in the hippocampus relative to controls (Fig. 8B, C). Furthermore, quantitative immunofluorescence microscopy revealed that clemastine treatment significantly increased the percentage of PV^+ inhibitory axons ensheathed by MBP^+ myelin (Fig. 8D–F). Collectively, these findings demonstrate that pharmacologically driving the myelination of inhibitory circuits is sufficient to elevate seizure thresholds, directly phenocopying the seizure resistance observed in the constitutive Gabrd-KO model.

Discussion

In this study, we evaluated the impact of global deletion of the γ-aminobutyric acid type A ($GABA_A$) receptor δ subunit, a core mediator of tonic inhibition, on brain excitatory/inhibitory (E/I) balance and seizure susceptibility. Contrary to the assumption that impaired inhibitory synaptic transmission invariably predisposes networks to hyperexcitability[18–21], we unexpectedly found that congenital *Gabrd* deficiency confers a distinct anti-ictogenic phenotype in mice. This resilience arises from widespread homeostatic remodeling within the central nervous system, initiated by the developmental loss of a key inhibitory component. Specifically, this homeostatic remodeling manifests at the cellular level through the expansion of the PV^+ interneuron subpopulation, and at the ultrastructural level via the targeted enhancement of myelination within inhibitory microcircuits. Single-cell interactome analysis further revealed that this targeted myelination is driven by the remodeling of neuronal-oligodendroglial communication, potentially mediated by the pleiotrophin (PTN) signaling axis. Furthermore, this structural compensatory is strictly dependent on a developmental window and is not effectively induced in the adult acquired TLE model. Together, these findings reveal an endogenous mechanism by which neural networks remodel E/I homeostasis through the targeted structural fortification of inhibitory circuits, and provide a proof-of-concept for pro-myelinating interventions (e.g., clemastine) applied during critical developmental window.

The δ subunit of the $GABA_A$ receptor is predominantly localized at extrasynaptic sites, where it finely tunes the neuronal resting membrane potential and firing threshold by mediating persistent tonic inhibition[4, 22]. The present study, together with previous reports, indicates that the electrophysiological consequences of *Gabrd* deficiency are highly cell-type specific[14, 23–25]. For instance, loss of the δ subunit in a $GAD65^+$ interneuron induces a state of disinhibition in inhibitory neurons[26]. The resulting increase in interneuron firing frequency compensatorily enhances phasic inhibition onto principal excitatory neurons (as reflected by increased sIPSC frequency and amplitude). Similarly, specific knockout of the δ subunit in PV^+ neurons of the medial prefrontal cortex (mPFC) led to aberrantly enhanced γ-band oscillations[27]. Collectively, these data support a model wherein *Gabrd* deficiency relieves interneuronal autoinhibition, thereby compensatorily strengthening specific patterns of inhibitory output at the circuit level.

In the context of global *Gabrd* knockout, both excitatory and inhibitory neurons are affected. Although baseline electroencephalographic monitoring indicated preserved resting E/I balance, these Gabrd-KO mice exhibited a distinct pharmacological profile: increased susceptibility to pentylenetetrazole (PTZ) [13] but pronounced tolerance to pilocarpine and kainic acid. This divergence likely reflects the distinct mechanisms of action of these convulsants and their interaction with the remodeled network. PTZ, a non-competitive antagonist, directly blocks intra-synaptic γ2-containing $GABA_A$ receptors[28, 29]. In Gabrd-KO mice, principal neurons already lack extrasynaptic δ-mediated tonic inhibition, the acute pharmacological blockade of residual phasic inhibition by PTZ causes rapid network collapse. In contrast, pilocarpine and KA induce seizures by imposing exogenous excitatory stimulation (activating M1 or KA receptors)[30, 31]. Under these conditions, the “disinhibited” and structurally expanded PV^+ network in Gabrd-KO mice exhibit higher recruitment efficiency, as evidenced by the marked upregulation of c-Fos in PV^+ neurons (Fig. S3), thereby providing stronger inhibition to counterbalance the excessive excitatory input.

It should be noted that while the circuit remodeling reduces seizure susceptibility under specific pathological stimuli, this homeostatic deviation does not equate to optimal physiological function. As shown in previous studies, Gabrd-KO mice exhibit significant anxiety-like behavior in the elevated plus maze[23], suggesting that this compensation represents a biological trade-off between reducing the risk of aberrant synchronous discharges and maintaining normal behavioral network dynamics. Furthermore, the present study demonstrates that the homeostatic remodeling is strictly restricted to a developmental window. Congenital *Gabrd* deficiency occurs during a period of high neural plasticity, allowing the network to recruit endogenous signaling pathways to drive microcircuit rewiring. In contrast, in the adult acquired TLE model,

Pathological *Gabrd* downregulation fails to trigger a compensatory expansion of PV^+ interneurons or a significant elevation in hippocampal myelination (Fig. 7). developmental "compensatory window" may partially explain the heterogeneity of clinical epilepsy penetrance: robust homeostatic remodeling during early development may mask underlying genetic susceptibility, whereas secondary pathological loss of inhibition in adulthood, occurring after the closure of the structural remodeling window, readily evolves into epilepsy.

The pivotal role of PV^+ interneurons in epileptic networks is well established[32, 33]; their optogenetic activation can directly abort aberrant discharge[34], whereas their progressive loss during chronic epilepsy drives hypersynchronization[35]. While our study revealed a significant expansion of PV^+ neurons in the Gabrd-KO hippocampus, proteomic analysis did not detect significant changes in the classical transcription factors governing PV^+ lineage specification (e.g., Nkx2.1, Lhx6)[36]. This suggesting that the expansion is not driven by cell-autonomous transcriptional reprogramming. Instead, intercellular communication analysis revealed substantial rewiring of the local microenvironment: the reception intensity of FGF signaling in the inhibitory neuron subpopulation (Cluster 6) was abnormally elevated; meanwhile, in the critical pathway regulating PV^+ neuron maturation and synaptogenesis (the

NRG signaling axis), downregulation of reception signals in other cell populations led to selective enrichment of paracrine signals toward inhibitory neurons. Thus, in the face of a global tonic inhibition deficit, the local microenvironment may drive compensatory expansion of PV^+neurons through selective redirection of neurotrophic and survival signals.

In parallel with interneuron expansion, our proteomic and ultrastructural analyses identified targeted hippocampal hypermyelination as a crucial component of the elevated seizure threshold. Notably, this myelin remodeling represents a local circuit adaptation rather than systemic white matter hyperplasia. Unlike the widespread corpus callosum thickening observed in whole-brain epilepsy models such as Wag/Rij rats or Scn8a mutants[37], the corpus callosum of Gabrd-KO mice in the present model remained structurally unperturbed (Fig. S4). Intercellular signaling analysis revealed enhanced paracrine signaling of PTN, a potent pro-oligodendrocyte differentiation factor, suggesting this localized myelin hypertrophy may be a coordinated network defense reaction triggered by altered electrical activity. Furthermore, recent studies have shown that extensive myelination of PV^+ neurons is essential for maintaining their high-frequency feedforward inhibition[16, 38, 39]. The targeted hypermyelination observed here likely serves to structurally and metabolically fortify these critical inhibitory pathways.

To establish whether enhanced myelination is sufficient to elevate seizure threshold, we treated wild-type mice with clemastine, a well-characterized agent that promotes oligodendrocyte precursor cell (OPC) differentiation[40, 41]. Previous studies have shown that in the *Adamts4* knockout model, early postnatal (P7-P15) administration of clemastine rescues aberrant mossy fiber development and reduces adult epileptic susceptibility[42]. Distinct from these acute pharmacological effects or early developmental rescue, the present study selected the postnatal time point of P28 in wild-type mice — a critical time point for synaptic maturation and extensive myelination of PV^+ neurons—for drug administration. The results showed that intervention within this time window not only successfully induced increased MBP expression and an increased number of myelinated PV^+ axons in the hippocampus of WT mice, but also significantly elevated seizure threshold. This dosing strategy effectively phenocopied the structural compensation and functional resistance observed in Gabrd-KO mice, while ruling out acute anti-inflammatory interference, thereby providing direct evidence that promoting PV-specific myelination during a defined developmental window represents a novel antiepileptic intervention strategy with high translational potential.

Extensive previous research demonstrates that the pharmacological efficacy of clemastine in driving OPC differentiation and myelination applies across a remarkably broad temporal window[43–46]. Within the context of epilepsy, recent study has shown that early administration of clemastine in *Adamts4* knockout mice can rescue aberrant OPC differentiation and mossy fiber sprouting, thereby reducing seizure susceptibility[42]. While this intervention primarily focused on rescuing early structural abnormalities, we synchronized our intervention with the developmental trajectory of neural circuits, targeting P28 (early adulthood). This period represents a critical checkpoint for the electrophysiological maturation of PV^+ interneurons. Between postnatal weeks 2 and 4, PV^+ neurons establish their signature

fast-spiking characteristics, evidenced by profound decreases in action potential duration and latency, alongside sharp increases in rheobase and firing frequency[47]. To support the high metabolic demands imposed by such high-frequency firing, the axonal myelination of these interneurons enters a crucial phase of expansion and stabilization from P22 to two months of age[48].

Building on this developmental trajectory, the core rationale of our study was to recruit the resident adult OPC pool to drive the adaptive myelination of functionally active PV^+ networks. Our experimental results support this hypothesis: clemastine administration during early adulthood significantly increased the number of myelinated PV^+ axons and successfully elevated the seizure threshold. These findings indicate that targeted pro-myelination of inhibitory axons represents a distinct antiepileptic strategy, one that proactively fortifies endogenous inhibitory circuit function through structural enhancement.

Although this study elucidates the endogenous mechanisms by which *Gabrd* deficiency triggers inhibitory circuit remodeling, several limitations remain. First, because the δ subunit is expressed across multiple neuronal subtypes, the global knockout model limits our ability to definitively determine whether the enhanced myelination of PV^+ neurons arises from cell-autonomous interneuron disinhibition or as a secondary consequence of altered principal neuron excitability. Second, the PTN signaling axis requires further validation through *in vivo* loss-of-function studies. Third, the lack of *in situ* molecular markers in TEM precludes the definitive distinction between excitatory and inhibitory axons mitochondrial aggregates Finally, the anxiety-like phenotypes associated with this remodeling underscore the need for future studies to rigorously evaluate the long-term cognitive and psychiatric impacts of pro-myelinating interventions prior to clinical translation.

In summary, this study reveals that congenital *Gabrd* deficiency drives remarkable resilience against epileptogenesis by triggering complex homeostatic rewiring within the brain. This protective effect is grounded in the targeted structural and myelinogenic fortification of PV^+ inhibitory microcircuits. Crucially, pharmacological intervention with a pro-myelinating agent during a critical developmental window successfully phenocopies the resistance, establishing that specific myelination of inhibitory microcircuits is a critical modulator of network excitability. These findings provide a novel translational avenue for the treatment of epilepsy.

Conclusions

This study reveals that congenital *Gabrd* deletion triggers homeostatic remodeling that paradoxically confers seizure resistance. This remodeling features expansion of PV^+ interneurons and selective enhancement of their axonal myelination, driven by PTN signaling. This compensation strictly depends on a developmental window and is absent in adult-acquired epilepsy. Pharmacologically promoting myelination with clemastine during the PV^+ maturation window phenocopies the protected state, establishing that structural fortification of inhibitory microcircuits critically modulates network excitability. These findings uncover an endogenous program for excitation/inhibition homeostasis and identify pro-myelinating intervention as a promising therapeutic strategy for refractory epilepsy.

Abbreviations

BCA
Bicinchoninic acid
DEPs
Differentially expressed proteins
DTT
Dithiothreitol
ECoG
Electrocorticogram
EEG
Electroencephalography
E/I
Excitatory/inhibitory
FDR
False discovery rate
FFT
Fast Fourier Transform
GABA
γ-aminobutyric acid
GABRD
$GABA_A$ receptor δ subunit
Gabrd-KO
Gabrd knockout
GEFS+
Generalized epilepsy with febrile seizures plus
GO
Gene Ontology
IAM
Iodoacetamide
ICA
Independent component analysis
JME
Juvenile myoclonic epilepsy
KA
Kainic acid
MBP
Myelin basic protein
mPFC
Medial prefrontal cortex

OPC
Oligodendrocyte precursor cell
PBS
Phosphate-buffered saline
PFA
Paraformaldehyde
PPI
Protein-protein interaction
PSD
Power spectral density
PTN
Pleiotrophin
PV^+
Parvalbumin-positive
RIPA
Radioimmunoprecipitation assay
SEM
Standard error of the mean
snRNA-seq
Single-nucleus RNA sequencing
TCA
Trichloroacetic acid
TEAB
Triethylammonium bicarbonate
TEM
Transmission electron microscopy
TMT
Tandem mass tag
WT
Wild-type

Declarations

Ethical Considerations

This study strictly adhered to the principles of the Declaration of Helsinki and the guidelines of the Guide for the Care and Use of Laboratory Animals. The study protocol was approved by the Ethics Committee of the First Affiliated Hospital of Xi'an Jiaotong University (Approval No.: LLSBPJ-2023-265).

Consent for publication

Not applicable

Availability of data and materials

The datasets are currently under further analysis and ongoing research, so public release is not feasible. Data are available from the corresponding author upon reasonable request.

Competing interests

The authors declare that they have no competing interests.

Funding

This study was supported by grants from the National Natural Science Foundation of China (Nos. 82101524 and 82371459), the Natural Science Basic Research Program of Shaanxi Province (No. 2023-JC-QN-0953), the Key Research and Development Program of Shaanxi Province (No. 2024SF-YBXM-216), and the Innovation Capability Support Program of Shaanxi Province (No. 2024LCZX-01).

Author's Contributions

LL wrote the original draft and performed the investigation. XZ performed the investigation. QM acquired funding and performed the investigation. HC performed formal analysis. XY developed the methodology. YL created the visualization. HL curated the data. YR provided resources. WW developed the methodology. HZ acquired funding and reviewed and edited the manuscript. HW conceived the study, supervised the work, and reviewed and edited the manuscript. All authors read and approved the final manuscript.

Acknowledgements

The authors thank the team members for their helpful comments, suggestions, and assistance during the research process.

References

1. Perucca E, White HS, Bialer M. New GABA-Targeting Therapies for the Treatment of Seizures and Epilepsy: II. Treatments in Clinical Development. CNS Drugs. 2023;37(9):781–95.
2. Sente A, et al. Differential assembly diversifies GABA(A) receptor structures and signalling. Nature. 2022;604(7904):190–4.
3. Leitch B. Parvalbumin Interneuron Dysfunction in Neurological Disorders: Focus on Epilepsy and Alzheimer's Disease. Int J Mol Sci, 2024. 25(10).
4. Farrant M, Nusser Z. Variations on an inhibitory theme: phasic and tonic activation of GABA(A) receptors. Nat Rev Neurosci. 2005;6(3):215–29.

5. Ahring PK, et al. Gain-of-function variants in GABRD reveal a novel pathway for neurodevelopmental disorders and epilepsy. Brain. 2022;145(4):1299–309.
6. Miller PS, et al. Structural basis for GABA(A) receptor potentiation by neurosteroids. Nat Struct Mol Biol. 2017;24(11):986–92.
7. Carver CM, Reddy DS. Neurosteroid Structure-Activity Relationships for Functional Activation of Extrasynaptic δGABA(A) Receptors. J Pharmacol Exp Ther. 2016;357(1):188–204.
8. Gilsoul M, et al. Subtle Brain Developmental Abnormalities in the Pathogenesis of Juvenile Myoclonic Epilepsy. Front Cell Neurosci. 2019;13:433.
9. Scheffer IE, et al. Neonatal epilepsy syndromes and generalized epilepsy with febrile seizures plus (GEFS+). Epilepsia. 2005;46:41–7.
10. Gallagher MJ, et al. The GABAA receptor alpha1 subunit epilepsy mutation A322D inhibits transmembrane helix formation and causes proteasomal degradation. Proc Natl Acad Sci U S A. 2007;104(32):12999–3004.
11. Peng Z, et al. Altered expression of the delta subunit of the GABAA receptor in a mouse model of temporal lobe epilepsy. J Neurosci. 2004;24(39):8629–39.
12. Dibbens LM, et al. GABRD encoding a protein for extra- or peri-synaptic GABAA receptors is a susceptibility locus for generalized epilepsies. Hum Mol Genet. 2004;13(13):1315–9.
13. Spigelman I, et al. Behavior and physiology of mice lacking the GABAA-receptor delta subunit. Epilepsia. 2002;43(Suppl 5):3–8.
14. Lee V, et al. Reduced tonic inhibition in the dentate gyrus contributes to chronic stress-induced impairments in learning and memory. Hippocampus. 2016;26(10):1276–90.
15. Cushman JD, et al. The role of the δ GABA(A) receptor in ovarian cycle-linked changes in hippocampus-dependent learning and memory. Neurochem Res. 2014;39(6):1140–6.
16. Maas DA, et al. Interneuron hypomyelination is associated with cognitive inflexibility in a rat model of schizophrenia. Nat Commun. 2020;11(1):2329.
17. Tadel F, et al. Brainstorm: a user-friendly application for MEG/EEG analysis. Comput Intell Neurosci. 2011;2011:879716.
18. Shen D, et al. De novo GABRG2 mutations associated with epileptic encephalopathies. Brain. 2017;140(1):49–67.
19. Minere M, et al. Presynaptic hyperexcitability reversed by positive allosteric modulation of a GABABR epilepsy variant. Brain. 2025;148(2):533–48.
20. Li R, et al. Transcriptionally downregulated GABAergic genes associated with synaptic density network dysfunction in temporal lobe epilepsy. Eur J Nucl Med Mol Imaging. 2025;52(6):1970–88.
21. Bakouh N, et al. Chloride deregulation and GABA depolarization in MTOR-related malformations of cortical development. Brain. 2025;148(2):549–63.
22. Nusser Z, Sieghart W, Somogyi P. Segregation of different GABAA receptors to synaptic and extrasynaptic membranes of cerebellar granule cells. J Neurosci. 1998;18(5):1693–703.

23. Rudolph S, et al. Cerebellum-Specific Deletion of the GABA(A) Receptor δ Subunit Leads to Sex-Specific Disruption of Behavior. Cell Rep. 2020;33(5):108338.
24. Melón LC, et al. Interneuronal δ-GABA(A) receptors regulate binge drinking and are necessary for the behavioral effects of early withdrawal. Neuropsychopharmacology. 2019;44(2):425–34.
25. Ferando I, Mody I. Altered gamma oscillations during pregnancy through loss of δ subunit-containing GABA(A) receptors on parvalbumin interneurons. Front Neural Circuits. 2013;7:144.
26. Lee V, Maguire J. Impact of inhibitory constraint of interneurons on neuronal excitability. J Neurophysiol. 2013;110(11):2520–35.
27. Ferando I, Mody I. vitro gamma oscillations following partial and complete ablation of δ subunit-containing GABAA receptors from parvalbumin interneurons. Neuropharmacology. 2015;88:91–8.
28. de Freitas RL et al. *μ(1) -Opioid receptors in the dorsomedial and ventrolateral columns of the periaqueductal grey matter are critical for the enhancement of post-ictal antinociception.* Synapse, 2016. 70(12): pp. 519–530.
29. Ramanjaneyulu R, Ticku MK. Interactions of pentamethylenetetrazole and tetrazole analogues with the picrotoxinin site of the benzodiazepine-GABA receptor-ionophore complex. Eur J Pharmacol. 1984;98(3–4):337–45.
30. Cavalheiro EA, et al. Spontaneous recurrent seizures in rats: amino acid and monoamine determination in the hippocampus. Epilepsia. 1994;35(1):1–11.
31. Hong JS, et al. Changes of hippocampal Met-enkephalin content after recurrent motor seizures. Nature. 1980;285(5762):231–2.
32. Wittner L, et al. Surviving CA1 pyramidal cells receive intact perisomatic inhibitory input in the human epileptic hippocampus. Brain. 2005;128(Pt 1):138–52.
33. Medici V, et al. Different parvalbumin and GABA expression in human epileptogenic focal cortical dysplasia. Epilepsia. 2016;57(7):1109–19.
34. Krook-Magnuson E, Soltesz I. Beyond the hammer and the scalpel: selective circuit control for the epilepsies. Nat Neurosci. 2015;18(3):331–8.
35. Colmers PLW et al. Loss of PV Interneurons in the BLA May Contribute to Altered Network and Behavioral States in Chronically Epileptic Mice. eNeuro, 2025. 12(1).
36. Du T, et al. NKX2.1 specifies cortical interneuron fate by activating Lhx6. Development. 2008;135(8):1559–67.
37. Knowles JK, et al. Maladaptive myelination promotes generalized epilepsy progression. Nat Neurosci. 2022;25(5):596–606.
38. Benamer N, et al. Myelination of parvalbumin interneurons shapes the function of cortical sensory inhibitory circuits. Nat Commun. 2020;11(1):5151.
39. Kole K, et al. Parvalbumin basket cell myelination accumulates axonal mitochondria to internodes. Nat Commun. 2022;13(1):7598.

40. Xie D, et al. Clemastine improves hypomyelination in rats with hypoxic-ischemic brain injury by reducing microglia-derived IL-1β via P38 signaling pathway. J Neuroinflammation. 2020;17(1):57.
41. Cooper JJM et al. *Clemastine Induces Oligodendrocyte Progenitor Pool Exhaustion and Senescence in the Context of Chronic Demyelination in a Rabbit Model.* Ann Neurol, 2024.
42. Jiang C, et al. Hippocampal Oligodendrocytes Regulate Mossy Fiber Development Involved in Epileptic Responses. Neurosci Bull. 2026;42(4):781–94.
43. Odell EP, et al. Minimum effective dose of clemastine in a mouse model of preterm white matter injury. Pediatr Res. 2024;96(4):933–41.
44. Green AJ, et al. Clemastine fumarate as a remyelinating therapy for multiple sclerosis (ReBUILD): a randomised, controlled, double-blind, crossover trial. Lancet. 2017;390(10111):2481–9.
45. Myatich A, et al. Clemastine in remyelination and protection of neurons and skeletal muscle after spinal cord injury. Neural Regen Res. 2023;18(5):940–6.
46. Chen JF, et al. Enhancing myelin renewal reverses cognitive dysfunction in a murine model of Alzheimer's disease. Neuron. 2021;109(14):2292–e23075.
47. Miyamae T, et al. Distinct Physiological Maturation of Parvalbumin-Positive Neuron Subtypes in Mouse Prefrontal Cortex. J Neurosci. 2017;37(19):4883–902.
48. Micheva KD, et al. Extensive Structural Remodeling of the Axonal Arbors of Parvalbumin Basket Cells during Development in Mouse Neocortex. J Neurosci. 2021;41(45):9326–39.

Figures

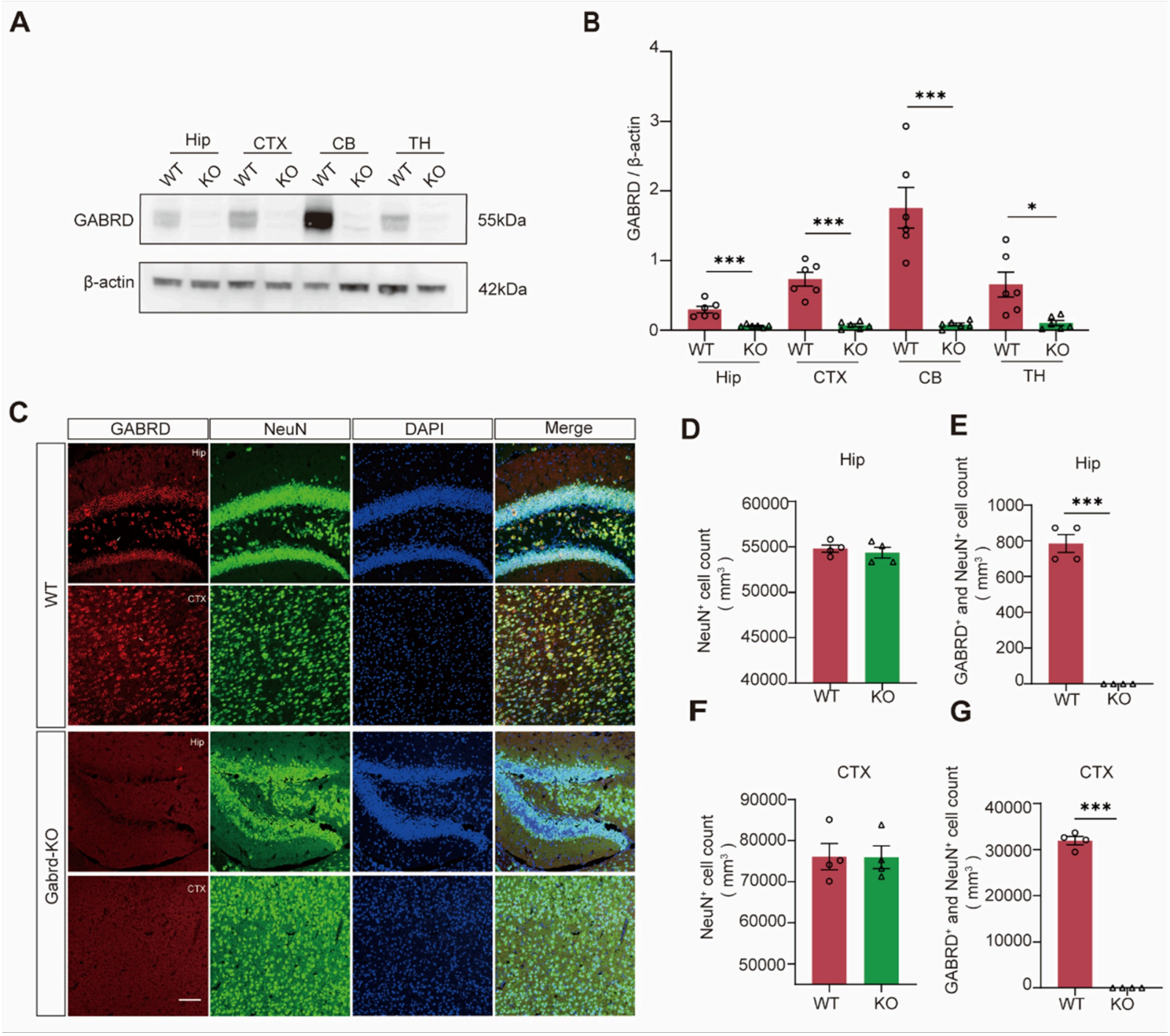


Figure 1

Validation of global Gabrd knockout (Gabrd-KO) mouse model. (A) Representative immunoblots of GABRD protein levels in lysates from the hippocampus, cortex, cerebellum, and thalamus of 8-week-old wild-type (WT) and Gabrd-KO mice. (B) Densitometric quantification of GABRD protein expression across brain regions (n = 6 per group). (C) Representative immunofluorescence images showing GABRD (red) and NeuN (green) distribution in the hippocampus and cortex of WT and Gabrd-KO mice (n = 4 per group). Scale bar = 100 μm. (D, E) Quantitative analysis of NeuN+ cell density and GABRD/NeuN colocalization in the hippocampus, and (F, G) in the cortex (n = 4 per group). Data are presented as mean ± SEM. Statistical significance was determined by unpaired t-test; *P < 0.05, ***P < 0.001.

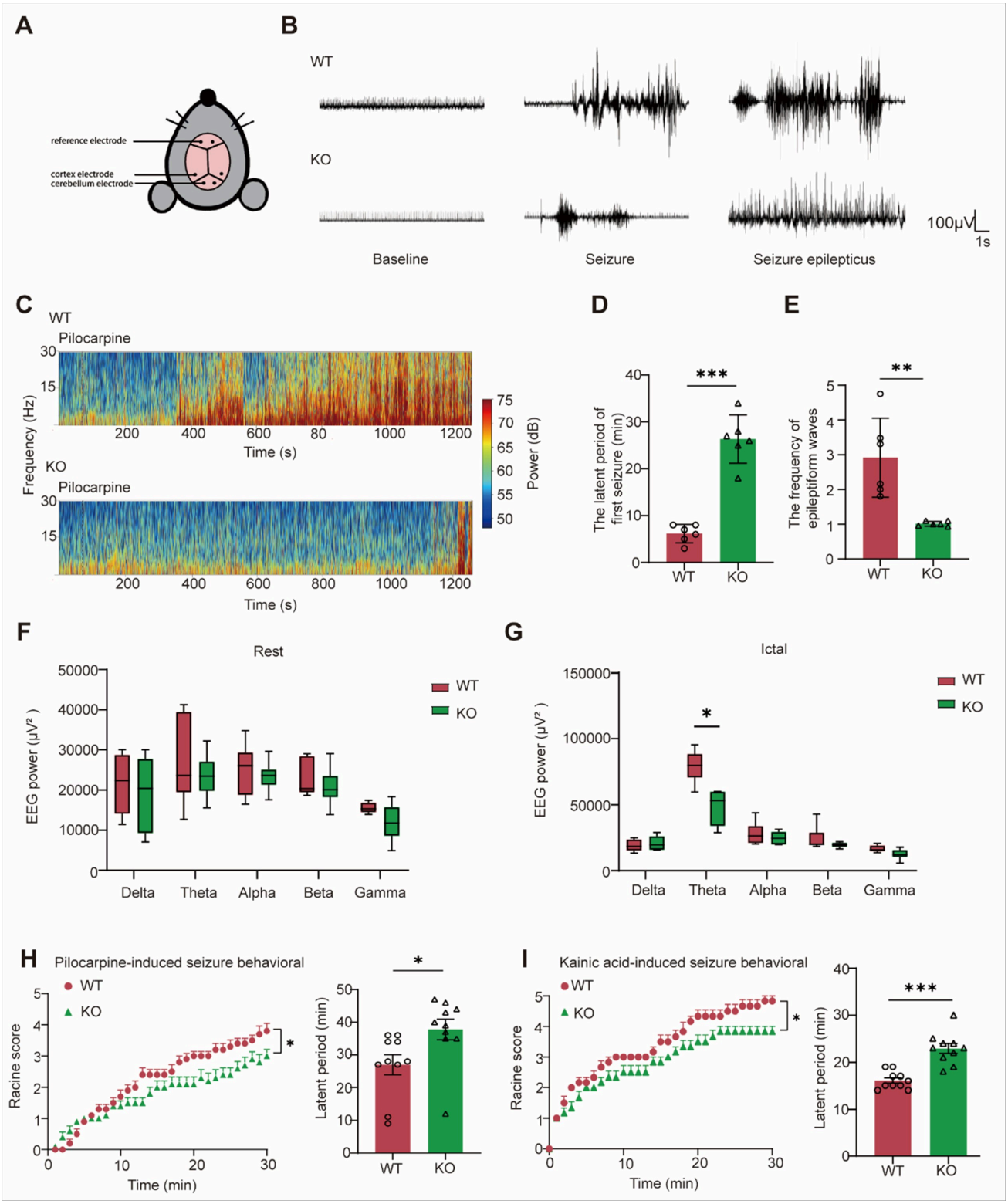


Figure 2

Gabrd deficiency confers resistance to chemoconvulsant-induced acute seizures. (A) Schematic diagram of electrode placement for in vivo electrocorticography (ECoG). The reference electrode was positioned bilaterally at the level of the nasion; unilateral recordings were used as the reference during data acquisition and analysis. (B) Representative ECoG traces from the two groups of mice during the resting state, acute seizure, and status epilepticus. (C) Time-frequency spectrograms transitioning from

the resting state to seizure onset following chemoconvulsant induction. (D) Quantification of latency to the first epileptiform discharge and (E) epileptiform discharge frequency during the 1-hour post-induction period (n = 6 per group). (F, G) Power spectral density (PSD) of ECoG activity during the resting state and ictal periods (n = 6 per group). (H, I) Time course of seizure severity (modified Racine scale) and quantification of latency to stage 4 seizures following systemic pilocarpine administration (H) and intrahippocampal kainic acid injection (I) (n = 10 per group). Data are presented as mean ± SEM. *P < 0.05, **P < 0.01, ***P < 0.001 (by unpaired two-tailed Student's t-test/Mann-Whitney U test).

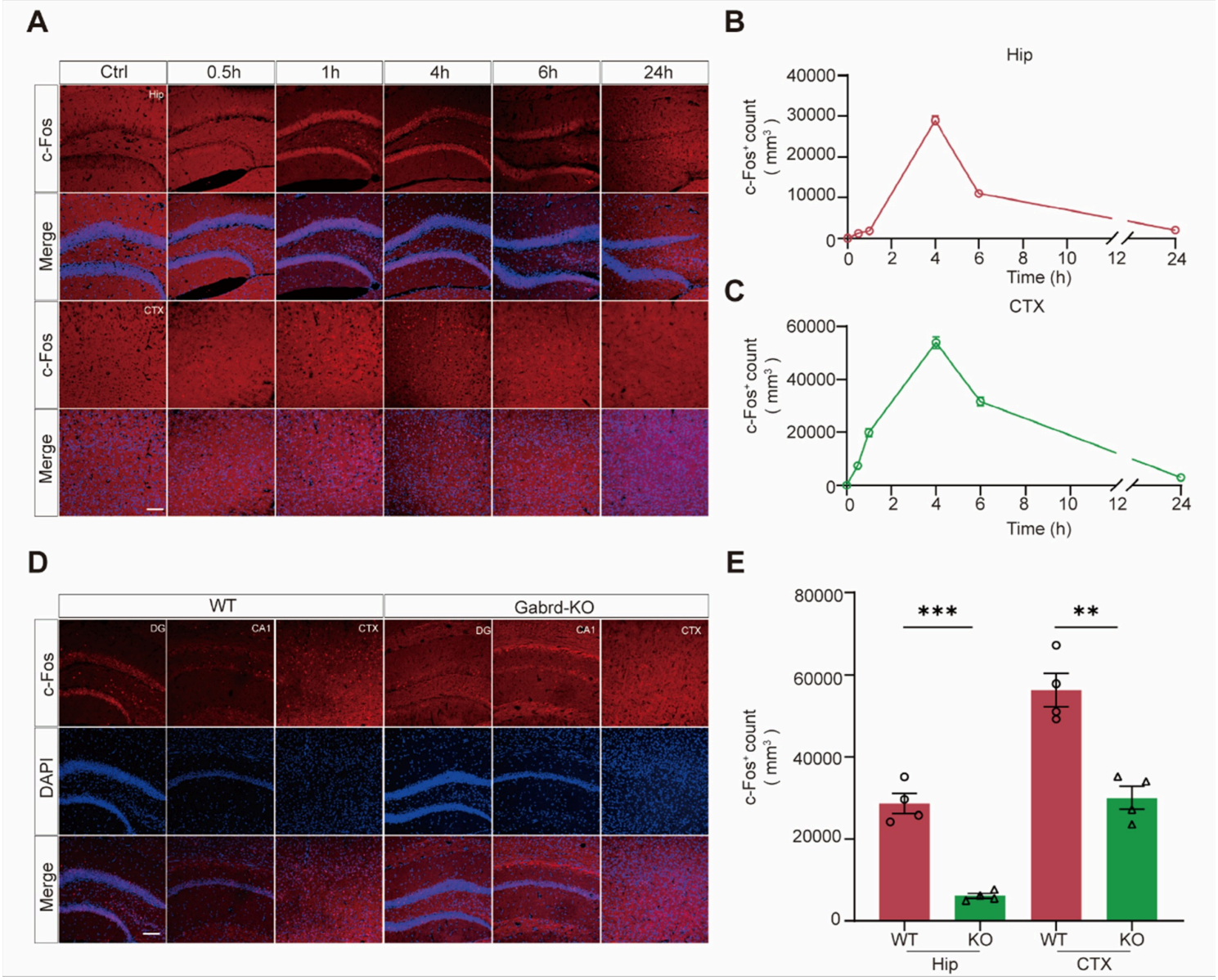


Figure 3

***Gabrd* deficiency attenuates seizure-induced c-Fos expression in the hippocampus and cortex.** (A) Representative confocal images of c-Fos immunofluorescence in brain tissue at different time points following seizure onset. (B, C) Time-course quantification of c-Fos$^+$ cells in the hippocampus (B) and cortex (C) of WT mice (n = 4 per time point). (D) Representative immunofluorescence images of c-Fos and DAPI co-labeling in the hippocampus and cortex of WT and Gabrd-KO mice at 4 h post-seizure. Scale

bar = 100 μm. (E) Quantification of c-Fos$^+$ cell counts in the hippocampus and cortex of WT and Gabrd-KO mice at 4 h post-seizure (n = 4 per group). Data are presented as mean ± SEM. ***P* < 0.01, ****P* < 0.001 (by unpaired two-tailed Student's t-test/Mann-Whitney U test).

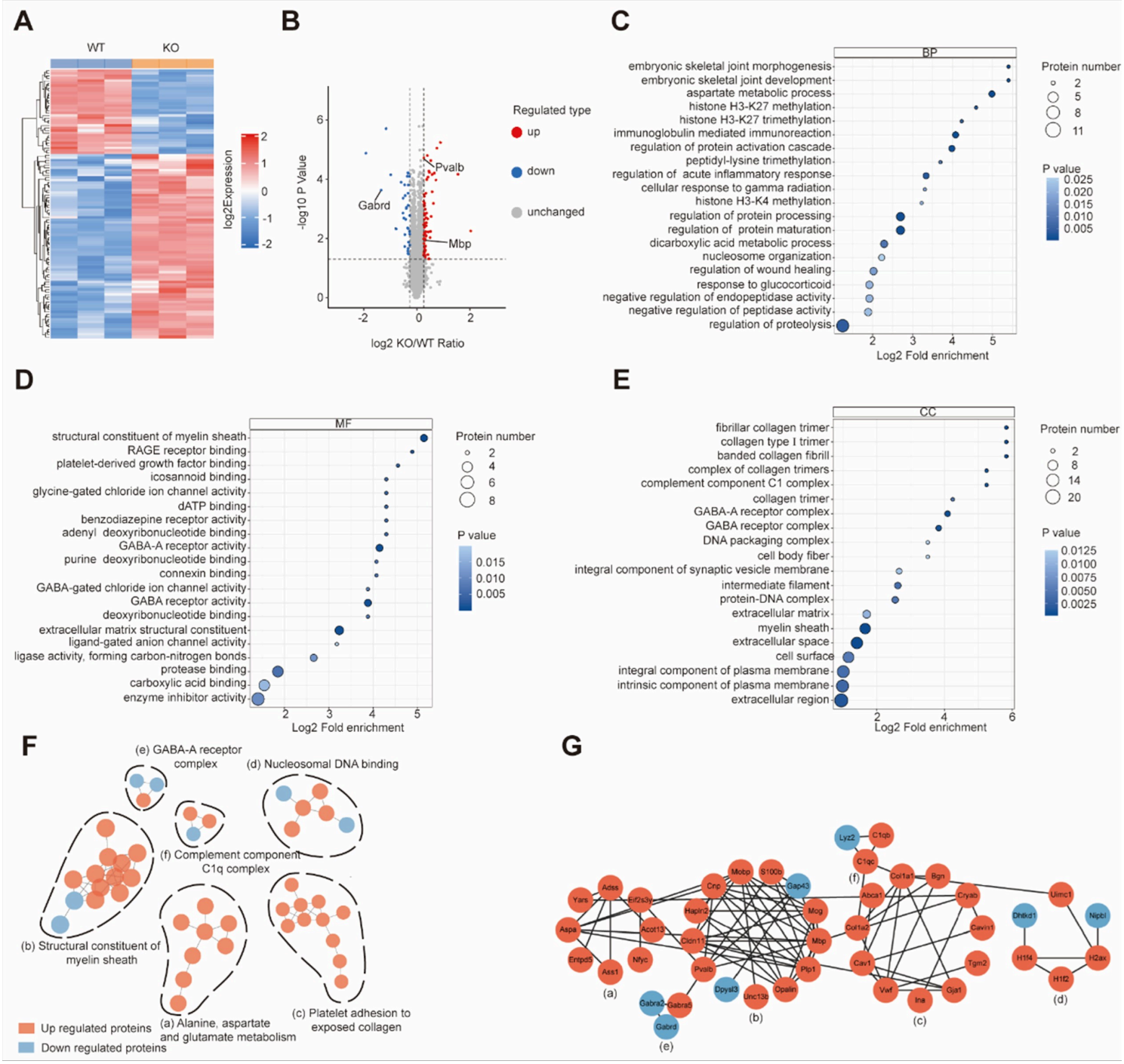


Figure 4

TMT-based quantitative proteomic profiling reveals myelin and GABAergic network remodeling in the Gabrd-KO hippocampus. (A) Hierarchical clustering heatmap of differentially expressed proteins (DEPs) in the hippocampus of Gabrd-KO versus WT mice. Red and blue indicate upregulated and downregulated protein abundance, respectively. (B) Volcano plot illustrating the distribution of DEPs. Red and blue data

points highlight significantly upregulated and downregulated proteins, respectively (threshold criteria: FC ≥ 1.2, FDR < 0.05). (C–E) Gene Ontology (GO) enrichment analysis of DEPs, showing the top significantly enriched terms in Biological Process (BP), Molecular Function (MF), and Cellular Component (CC) categories, respectively. (F) Protein-protein interaction (PPI) network of the DEPs. Node colors indicate upregulation (orange) or downregulation (blue) in Gabrd-KO mice relative to WT mice. (G) Interconnections among major functional modules extracted from the PPI network.

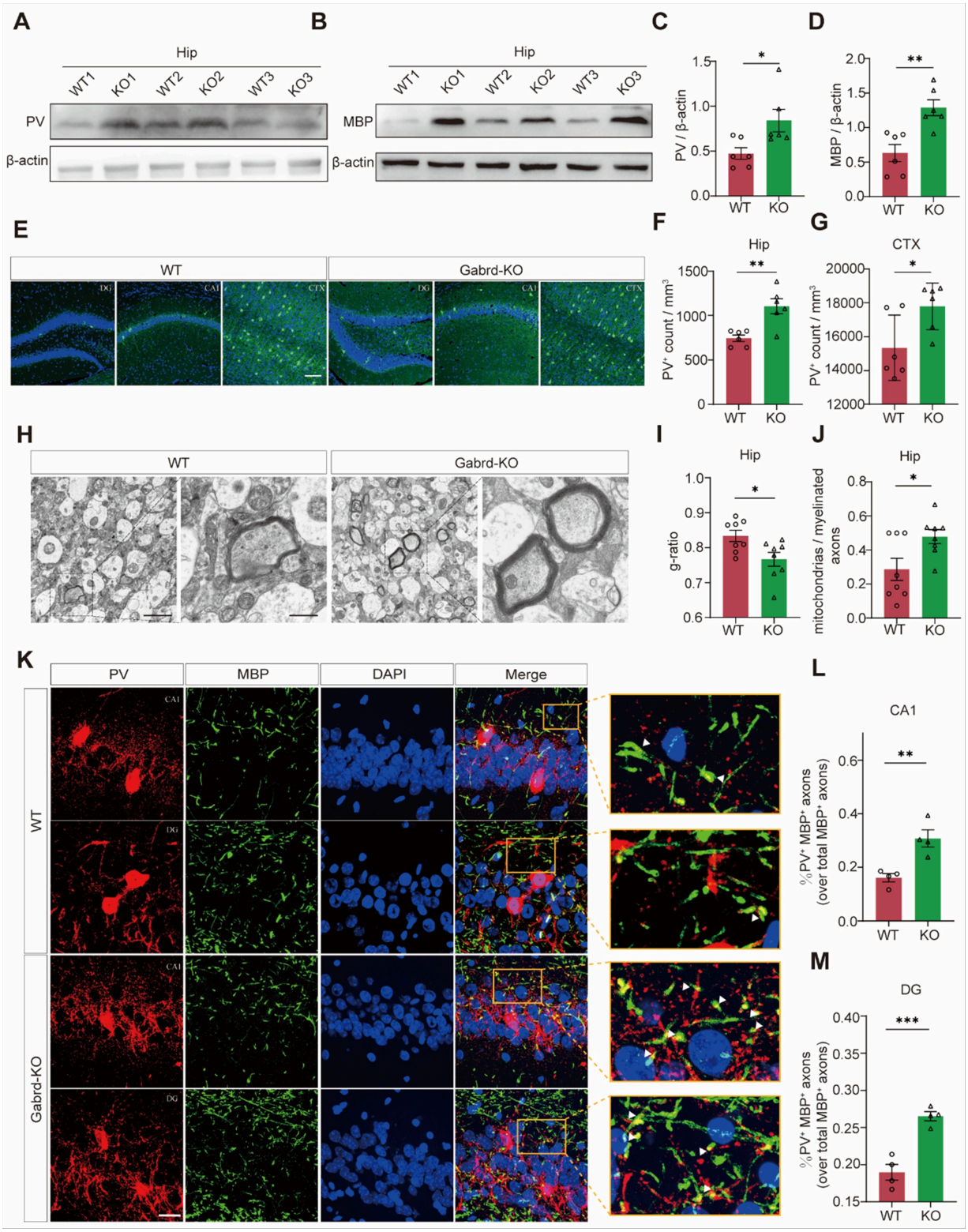


Figure 5

Validation of PV and MBP upregulation and ultrastructural myelin remodeling in the Gabrd-KO hippocampus. (A, B) Representative immunoblots of parvalbumin (PV; A) and myelin basic protein (MBP; B) in hippocampal lysates from WT and Gabrd-KO mice. (C, D) Densitometric quantification of PV and MBP protein expression levels (n = 6 per group). (E) Representative immunofluorescence images of PV^+ (red) and DAPI (blue) staining in the hippocampus and cortex of WT and Gabrd-KO mice. Scale bar = 100 μm. (F, G) Quantitative analysis of PV^+ cell density in the hippocampus and cortex of WT and Gabrd-KO mice (n = 6 per group). (H) Transmission electron microscopy ultrastructural (TEM) images of hippocampal myelinated axons from WT and Gabrd-KO mice. Left scale bar = 5 μm; right scale bar = 1 μm. (I, J) Quantification of myelin g-ratio (I) and mitochondria within hippocampal myelinated fibers (J) (n = 8 per group). (K) Representative immunofluorescence images detailing PV (red) and MBP (green) co-localization in the hippocampus. Scale bar = 20 μm. (L, M) Quantification of the percentage of PV^+ axons ensheathed by MBP^+ myelin in the hippocampal CA1 and DG regions (n = 4 per group). Data are presented as mean ± SEM. **P* < 0.05, ***P* < 0.01, ****P* < 0.001 (by unpaired two-tailed Student's t-test/Mann-Whitney U test).

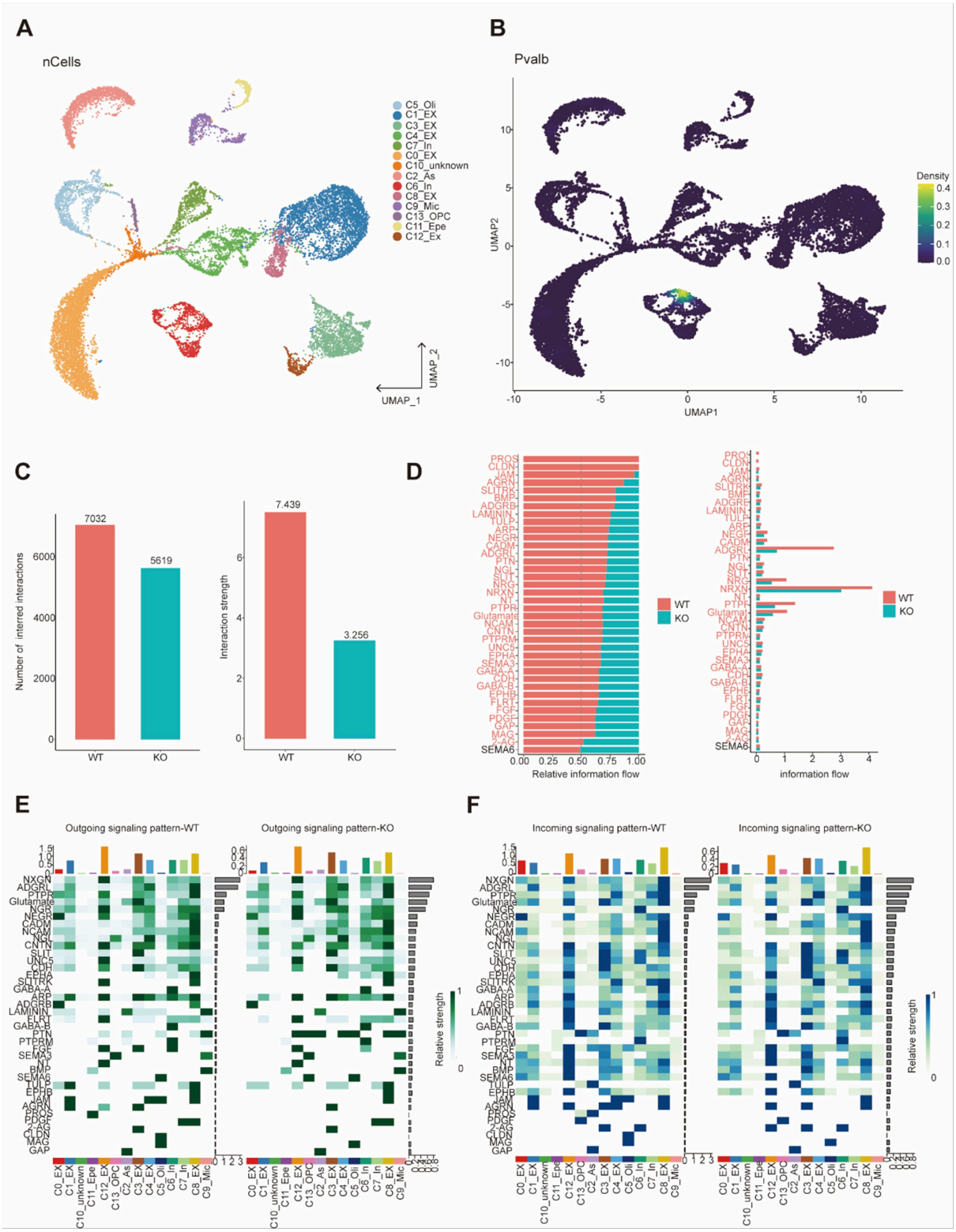


Figure 6

Single-nucleus transcriptomics reveals global attenuation and selective remodeling of hippocampal intercellular communication in Gabrd-KO mice. (A) Uniform Manifold Approximation and Projection (UMAP) embedding of 14 distinct cell clusters identified in the hippocampus of WT and Gabrd-KO mice. (B) Feature plot highlighting the distribution and relative expression of *Pv* mRNA across the identified cell clusters. (C) Quantification of the total number of inferred intercellular signaling interactions (left)

and overall communication strength (right) in the hippocampus of WT and Gabrd-KO mice. (D) Information flow analysis comparing signaling pathway probabilities between genotypes, displayed as proportional distribution (left) and absolute differences (right). Pathways with significantly higher communication strength in WT mice (defined asa total pathway probabilities ration (Gabrd-KO/WT) < 0.95; $P < 0.05$, non-parametric rank-sum test) are highlighted in red, whereas those with no significant difference are in green. (E) Heatmap detailing outgoing (E) and incoming (F) signaling patterns across specific cell subpopulations. Color intensity correlates with communication strength. Marginal histograms represent cumulative signaling intensity along the vertical and horizontal axes.

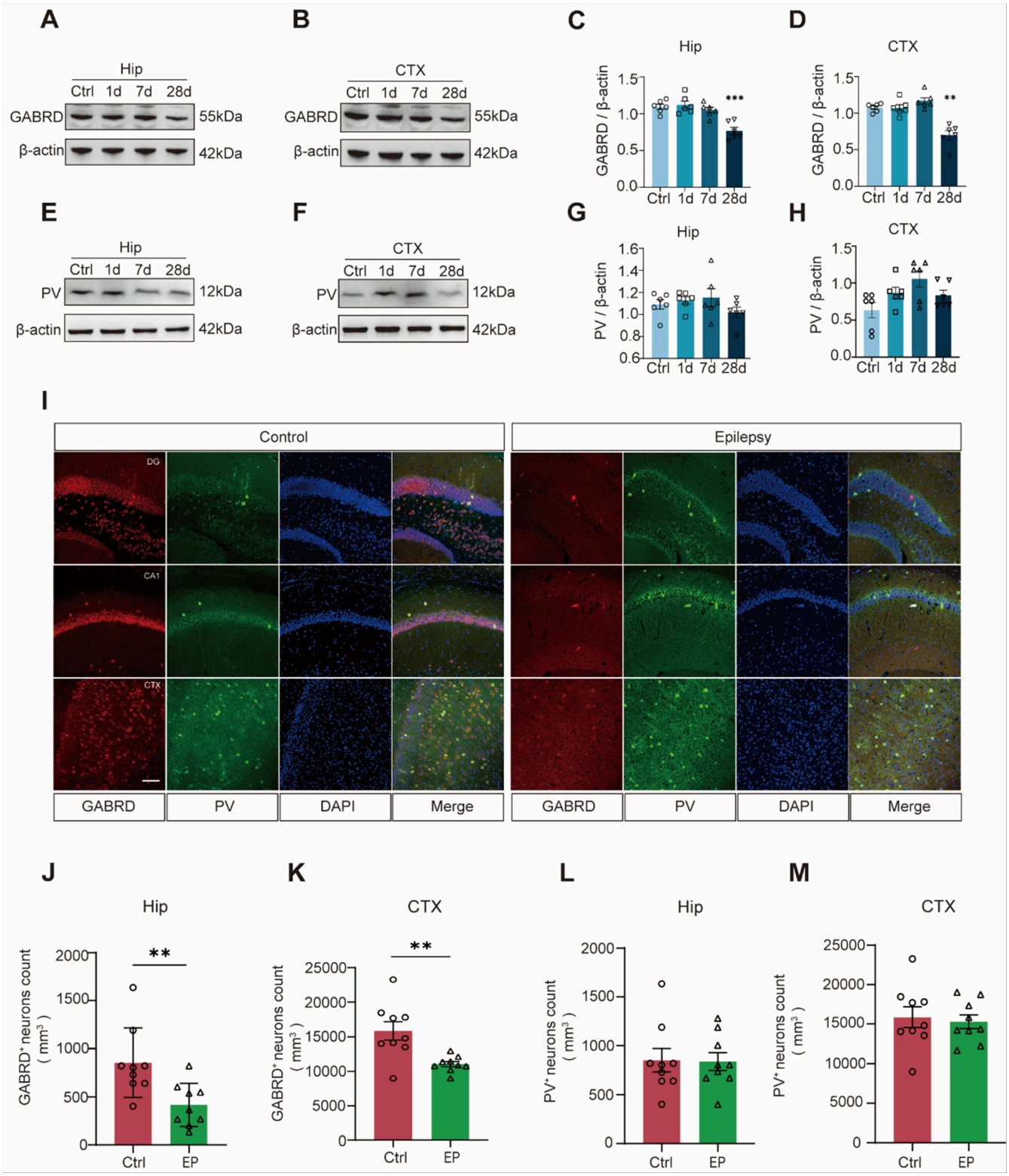


Figure 7

Disease-associated GABRD downregulation in acquired TLE does not elicit PV upregulation. (A, B) Representative immunoblots of GABRD in the hippocampus (A) and cortex (B) of control mice and acquired TLE mice at 1-, 7-, and 28-days following pilocarpine-induced status epilepticus. (C, D) Densitometric quantification of GABRD protein levels in the hippocampus and cortex (n = 6 per group). (E, F) Representative immunoblots of PV in the hippocampus (E) and cortex (F) across the indicated

temporal stages of epileptogenesis. (G, H) Densitometric quantification of PV protein levels (n = 6 per group). (I) Representative immunofluorescence images of GABRD and PV co-labeling in the hippocampus and cortex at day 28 post-status epilepticus. Scale bar = 100 μm. (J, K) Quantitative analysis of GABRD-positive cell density in the hippocampus (J) and cortex (K) of both groups at day 28 (n = 9 per group). (L, M) Quantitative analysis of PV^+ cell density in the hippocampus (L) and cortex (M) of both groups (n = 9 per group). Data are presented as mean ± SEM. *P < 0.05, **P < 0.01, ***P < 0.001 (by one-way ANOVA followed by post hoc tests for C, D, G, H; and unpaired two-tailed Student's t-test/Mann-Whitney U test for J, K, L, M).

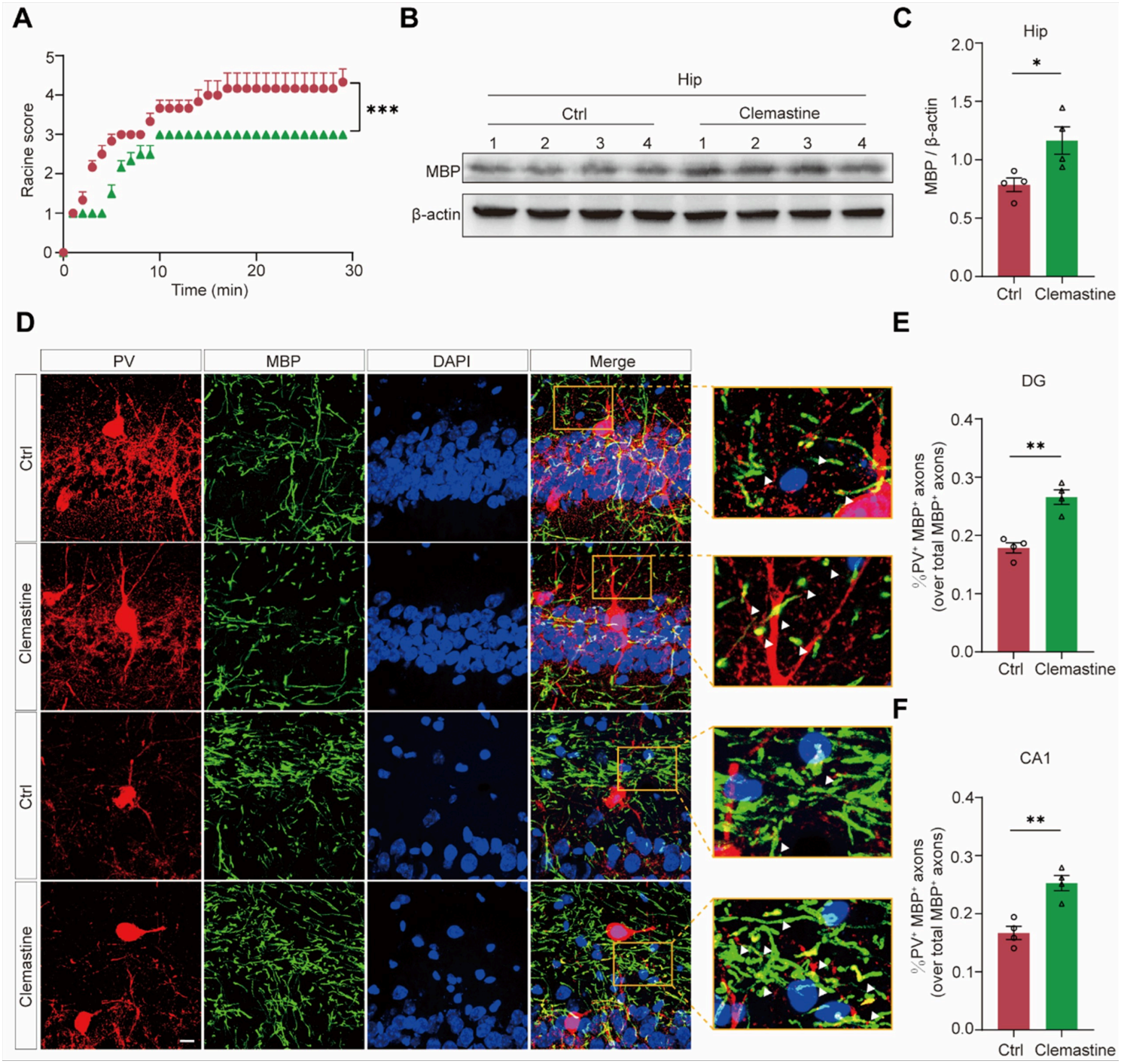


Figure 8

Pharmacological induction of myelination elevates seizure thresholds in WT mice. (A) Quantification of behavioral seizure scores and latency in chemoconvulsant -induced epilepsy models for control and clemastine-treated mice (n = 10 per group). (B) Representative immunoblots of MBP protein in the hippocampus of control (vehicle-treated) and clemastine-treated WT mice with treatment initiated at postnatal day 28 (P28). (C) Densitometric quantification of MBP protein levels in the P28 (n = 4 per group). (D) Representative immunofluorescence images of PV (red) and MBP (green) co-labeling in the hippocampus of control and clemastine-treated mice. Scale bar = 20 μm. (E, F) Quantitative analysis of the percentage of PV^+ axons ensheathed by MBP^+ myelin in the hippocampal CA1 and DG regions (n = 4 per group). Data are presented as mean ± SEM. **P* < 0.05, ***P* < 0.01, ****P* < 0.001 (by unpaired two-tailed Student's t-test/Mann-Whitney U test).

Supplementary Files

This is a list of supplementary files associated with this preprint. Click to download.

- supplementarymaterials.docx
- SupplementalMaterials.docx